Newtonian Radial Entrance Flow

Ajay Chatterjee
Dept. of Chemical Engineering, Indian Institute of Technology Delhi, New Delhi 110016, India

The laminar flow of a Newtonian fluid is considered through a prototype radial entrance geometry that consists of a circular pipe joined to the bottom plate of a pair of parallel circular plates, a configuration that mimics and idealizes important practical flows. The equations of motion are solved numerically to compute the velocity field as a function of the Reynolds number Re and the geometrical aspect ratio e. This work extends limited previous results on flow development in this entrance geometry. A range of e and Re are considered, and the Re−e parameter space corresponding to flow separation is delineated. The computed results are used to illustrate the role of the aspect ratio in influencing flow development for small $e \lesssim 1$ *and are analyzed to quantify the large e asymptotic behavior of various quantities characterizing the developing flow field. The limiting value of aspect ratio beyond which the asymptotic behavior applies is relatively small* $e \gtrsim 2$. *The dependence of these quantities on Re also is analyzed. The results are discussed in light of available experimental measurements and existing analytical results. An important implication of the results in the context of confined laminar impinging jet heat transfer is described. The entrance configuration is contrasted with a companion radial entrance flow (radial source flow); although flow separation occurs in both cases, some basic features are quite distinct. The influence of the elongational character of this radial flow field is highlighted by comparing certain aspects of flow development between this axisymmetric configuration and its 2-D Cartesian analog.*

Introduction

This work investigates flow development in a prototype radial entrance flow. The geometry is depicted in Figure 1 and consists of a circular pipe of radius R connected to the bottom plate of a pair of parallel circular plates that are a distance L apart, with $e = L/R$ being the geometrical aspect ratio. The region between the plates forms the channel for the radial outward flow of the fluid. Fluid enters the circular pipe axially at $z = -\infty$, encounters the entrance region at $z = 0$, and subsequently exits the flow field radially at $r = \infty$. Fully developed velocity profiles are imposed at the entrance and exit planes. The flow in this geometry is governed by two dimensionless parameters, the aspect ratio e just defined and the Reynolds number $Re = 2RU\rho/\mu$, where the physical parameters all have their usual meaning and U is the average axial velocity in the pipe.

This flow field mimics and idealizes flow configurations of interest in semiconductor processing (Hollahan and Rosler, 1978; Reinberg, 1979) and polymer processing (Middleman, 1977), in biological studies (Goetz et al., 1994), in the investigation of membrane transport processes (Camera-Roda et al., 1994), and in heat transfer with confined impinging jets (Behnia et al., 1999). At the inlet plane $z = -\infty$ the fluid is in simple shear flow and satisfies the classic parabolic velocity profile for steady flow in a pipe. On the other hand, at the exit plane $r = \infty$ the deformation field is the sum of a simple shear flow due to the circular plate surfaces, and an elongation flow due to the varying cross-sectional area, with the elongation component ($\sim r^{-2}$) decaying faster than the shear component ($\sim r^{-1}$). When inertia is neglected, as is reasonable at large radial distances, the well-known creeping-flow radial velocity profile emerges with a parabolic variation in z and an r^{-1} dependence on the radial coordinate. In the entrance region surrounding $z = 0$ the flow field adjusts between these limiting distributions.

Some limited analysis of this complete flow field has been presented previously using both a numerical (Chatterjee and White, 1989), and an analytical (Chatterjee, 1993) approach valid in the slow-flow limit. Substantial upstream flow devel-

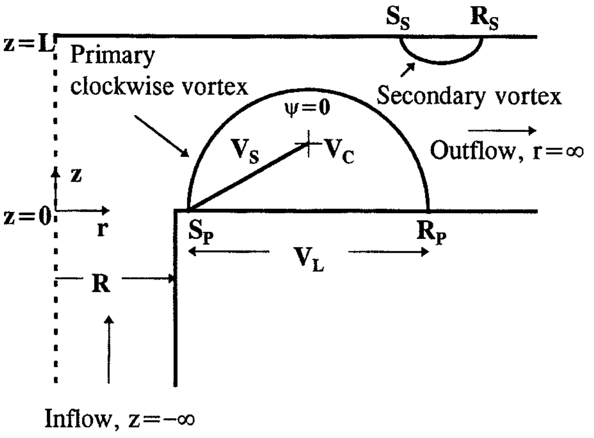

Figure 1. Axisymmetric radial entrance flow geometry and its basic flow features.

opment occurs at low Reynolds numbers, and for $Re = 0$, $e = 1/4$, this leads to an entirely nonparabolic axial velocity profile at the plane $z = 0$, which shows a well-defined off-centered maximum (at $r = \sim 0.85R$) along with a minimum at $r = 0$. This concavity in the axial velocity profile at the entrance plane $z = 0$ obviously has nothing to do with fluid inertia. Unlike the situation in other entrance flows (for instance, the sudden contraction geometry), it is entirely a consequence of axial-vorticity diffusion. The principal feature at nonzero Reynolds numbers in this flow field is the presence of flow separation near the sharp corner $r = R$, $z = 0$. The consequent primary vortex, which is clockwise in the sketch in Figure 1 because the main flow driving the vortex traverses from left ($r = 0$) to right ($r = \infty$), grows as a function of the aspect ratio and the Reynolds number.

Limited results of the previous analyses indicate that for the values of parameters (Re and e) considered, attainment of the fully developed radial velocity distribution is completed typically within a few pipe radii from the sharp corner $r = R$, $z = 0$ in the creeping-flow limit, but occurs over longer distances at nonzero Reynolds numbers. Thus, the calculated dimensionless radial entrance length (scaled with R) is larger at nonzero Reynolds number due to the growth of the clockwise vortex. In qualitative agreement with experimental data (Jackson and Symmons, 1965), a calculation of the midplane ($z = L/2$) radial pressure profile at $Re = 200$, $e = 1$ reveals its significant departure from the fully developed logarithmic profile, thus prompting the observation that notwithstanding their success at very small aspect ratios (Moller, 1963; Chen, 1966), perturbations about the inertia free limit (Hunt and Torbe, 1962; Jackson and Symmons, 1965) cannot adequately describe the nonzero Reynolds number flow features in this geometry at moderate to large aspect ratios. As has been mentioned earlier (Chatterjee and White, 1989), the success at small aspect ratios is a consequence of the dominance of axial vorticity diffusion at low e, which tends to restore the effects of viscous dissipation throughout the flow. Furthermore, as emphasized in Raal (1978) these perturbation solutions do not apply in the region where the flow is shaped by the entrance conditions.

The principal objective here is to obtain a more complete account of the structure of the developing flow field with a view toward quantifying the dependence of various quantities (entrance length, vortex size and strength, excess pressure loss) on the aspect ratio and the Reynolds number. The earlier numerical article provided only a limited set of results for this entrance flow field and discussed the basic flow features in a qualitative manner without examining the flow structure systematically and quantitatively, as the aspect ratio and the Reynolds number are varied over a broad range of values. As the aspect ratio is increased to large values, the flow in the pipe assumes an invariant form and the pipe radius R is relevant only insofar as to specify the incoming velocity distribution at the plane $z = 0$. A scaling with L of the governing equations then suggests that at a fixed Reynolds number derived quantities such as the entrance length and the vortex size must be $O(1)$ at leading order, or equivalently behave as $O(e)$ when they are nondimensionalized with R. Our numerical computations indicate that a simple linear scaling with e can describe this asymptotic behavior that applies at aspect ratios $e \gtrsim 2$. The properties of the primary clockwise vortex that dominates the developing flow field at high aspect ratios and nonzero Reynolds numbers undoubtably are of some intrinsic interest, but they are also relevant in practical situations involving the transport and reaction of species wherein the size and strength of the vortex may be an important variable in correlating mass transfer and reaction rates. We tabulate extensive results for these properties and discuss their behavior as a function of the aspect ratio and the Reynolds number. Detailed results are also presented for the excess pressure loss in this radial entrance geometry, and it is observed that at a given nonzero Reynolds number the excess pressure loss is not a monotonic function of the aspect ratio due to the occurrence of flow separation and consequent growth of the clockwise vortex as the aspect ratio is increased.

Apart from its relevance in the situations just mentioned, one other reason for focusing on this flow field is that in a manner analogous to the sudden contraction geometry (Boger, 1987), this entrance configuration can serve as a prototype radial entrance flow field. To this end we contrast certain features of this radial entrance flow with radial source flow (Raal, 1978), which also involves a developing radial flow field, but with an entrance configuration that is perhaps somewhat more artificial than the present situation. A third reason for studying this developing flow is related to the analysis of thermal development and heat transfer in this geometry. In the forced convection limit for a constant property fluid the velocity field enters as a known field variable in the energy equation; consequently, a critical understanding of the flow field is necessary in order to interpret the developing temperature field.

As noted earlier, this geometry is relevant in the context of heat transfer in confined impinging jets. Much of the published analysis of confined laminar impinging-jet heat transfer has tended to favor the corresponding two-dimensional (2-D) Cartesian configuration (Al-Sanea, 1992), although the present axisymmetric configuration also has been considered, a recent contribution being the article by Lee et al. (1997). These articles are not focused on a detailed and systematic analysis of the developing flow field, their attention largely being directed toward computing and correlating the Nusselt number variation along the surface $z = L$. In addition, by assigning a flat or a parabolic form for the axial velocity distribution at the plane $z = 0$, these analyses invariably have restricted their computation to the region $z > 0$.

Analysis of heat transfer in the 2-D Cartesian geometry, for both the unconfined (Sparrow and Lee, 1975) and the confined (Al-Sanea, 1992; Schafer et al., 1992) configurations, has shown that the local Nusselt number in the neighborhood of the stagnation point ($r = 0$, $z = L$ in this axisymmetric configuration) is a strong function of the precise shape of the axial velocity distribution at the plane $z = 0$. Consequently, it is desirable to know under what conditions upstream flow development can be ignored so that a given form (say parabolic) for the axial velocity profile can be prescribed at the plane $z = 0$. When the pipe is long enough (much longer than $\sim 0.1\,Re$ in terms of its radius (Vrentas and Duda, 1973) if the fluid is fed from a reservoir), then the axial velocity distribution in the pipe upstream of the plane $z = 0$ will be parabolic, but whether it will remain parabolic at $z = 0$ depends on both Re and e. We use our results to establish quantitative limiting values of the parameters Re and e, which ensures this possibility. When these conditions are satisfied, it will be reasonable to impose a parabolic axial velocity distribution at $z = 0$ and neglect flow development in the region $z \leq 0$. On the other hand, we also show that, for small $e \lesssim 1$ vorticity, diffusion will distort the shape of the axial velocity profile at the plane $z = 0$ regardless of the value of Re. Hence, for aspect ratios $e \lesssim 1$, imposition of the parabolic profile (or indeed some other arbitrary form) for the axial velocity at the plane $z = 0$ will be incorrect even at large Reynolds numbers.

In summary, in this article we reconsider the steady flow of a Newtonian fluid of constant physical properties in this radial entrance geometry by employing the complete equations of motion. We consider a broad range of parameter values Re and e and focus our calculations on a quantitative understanding of the behavior of the developing flow field as a function of Re and e.

Governing Equations and Numerical Techniques

A few pertinent remarks regarding the governing field equations and the numerical techniques adopted in this work are reviewed here, and additional details can be found in an earlier numerical article (Chatterjee and White, 1989). This entrance flow domain extends to infinity in both the axial and radial directions, which presents a difficulty with elliptic equations. A common approach in this regard is to map the infinite domain to a finite region through the use of fairly standard transformations. In this spirit we apply the exponential transformation to the radial coordinate, thus $\chi = 1 - e^{-\beta\xi}$, where ξ is the scaled radial coordinate ($\xi = r/R$). Now as ξ varies from 0 to ∞, the transformed coordinate χ goes from 0 to 1. β is a stretching factor that can be varied to modulate the radial grid size in the physical (r, z) coordinate system, and its numerical value must be chosen small enough to provide adequate radial resolution along the physical coordinate (r, or equivalently ξ) since the physical grid size scales as $\Delta\xi = (\exp(\beta\xi)/\beta)\Delta\chi$. The axial coordinate does not present a significant problem because the pipe can be conveniently truncated at $z/R \simeq 2$, since upstream flow development in the pipe typically is expended within two pipe radii from the entrance plane $z = 0$ for the smallest aspect ratio considered in this study. The unfortunate consequence of applying the exponential transformation is that the field equations now are somewhat more complex, and they are collected here for convenient reference. In the earlier numerical study the exponential transformation was not employed.

1. The stream function equation:

$$\beta^2(1-\chi)^2\frac{\partial^2\psi}{\partial\chi^2} - \beta^2(1-\chi)\frac{\partial\psi}{\partial\chi} + \frac{\beta^2(1-\chi)}{\ln(1-\chi)}\frac{\partial\psi}{\partial\chi} + \frac{\partial^2\psi}{\partial\eta^2} = -\frac{\ln(1-\chi)}{\beta}\omega. \qquad (1)$$

2. The vorticity transport equation:

$$-\frac{\beta^2\omega\dfrac{\partial\psi}{\partial\eta}}{[\ln(1-\chi)]^2} - \frac{\beta^2(1-\chi)}{\ln(1-\chi)}\frac{\partial\omega}{\partial\chi}\frac{\partial\psi}{\partial\eta} + \frac{\beta^2(1-\chi)}{\ln(1-\chi)}\frac{\partial\omega}{\partial\eta}\frac{\partial\psi}{\partial\chi}$$

$$= \frac{2}{Re}\left\{\beta^2(1-\chi)^2\frac{\partial^2\omega}{\partial\chi^2} - \beta^2(1-\chi)\frac{\partial\omega}{\partial\chi} - \frac{\beta^2(1-\chi)}{\ln(1-\chi)}\frac{\partial\omega}{\partial\chi} - \frac{\beta^2\omega}{[\ln(1-\chi)]^2} + \frac{\partial^2\omega}{\partial\eta^2}\right\}. \qquad (2)$$

In these equations ψ and ω represent the dimensionless stream function and vorticity that are related in the usual way to the dimensionless radial and axial velocity components:

$$u_\chi = -\frac{\beta}{\ln(1-\chi)}\frac{\partial\psi}{\partial\eta}; \qquad u_\eta = \beta^2\frac{1-\chi}{\ln(1-\chi)}\frac{\partial\psi}{\partial\chi};$$

$$\omega = \frac{\partial u_\chi}{\partial\eta} - \beta(1-\chi)\frac{\partial u_\eta}{\partial\chi},$$

where the velocities are made dimensionless with the average axial velocity in the pipe; χ and η ($= z/R$) are the dimensionless radial and axial coordinates in the transformed computational domain; and Re is the Reynolds number. In the region $z > 0$, we scale the axial variable with L, so that $\eta^* = z/L$, and incorporate the aspect ratio e in the governing equations for this region. With this revised scaling for the axial variable, the plate surface $z = L$ is fixed at $\eta^* = 1$ regardless of the value of e. The boundary data on the stream function and vorticity reflect the assumption of fully developed velocity profiles at the inlet ($z = -\infty$) and exit ($r = \infty$) planes, no slip and no penetration at solid surfaces, and the axisymmetric nature of the flow field. They are given below for completeness.

Boundary conditions on the stream function and vorticity:

$$\psi = \frac{1}{2} + \xi^2\left[\frac{\xi^2}{2} - 1\right], \quad \omega = 4\xi; \quad \text{for } \eta \to -\infty,\ 0 \le \xi \le 1$$

$$\psi = \frac{1}{2}, \quad \omega = 0; \quad \text{for } \xi = 0,\ -\infty < \eta \le 0$$

$$\psi = \frac{1}{2}, \quad \omega = 0; \quad \text{for } \xi = 0,\ 0 \le \eta^* \le 1$$

$$\psi = 0, \quad \frac{\partial \psi}{\partial \xi} = 0; \quad \text{for } \xi = 1;\ -\infty < \eta \le 0$$

$$\psi = 0, \quad \frac{\partial \psi}{\partial \eta} = 0; \quad \text{for } \eta = \eta^* = 0,\ 1 \le \xi < \infty$$

$$\psi = \frac{1}{2}, \quad \frac{\partial \psi}{\partial \eta} = 0; \quad \text{for } \eta^* = 1,\ 0 \le \xi < \infty$$

$$\psi = 3\left[\frac{\eta^{*2}}{2} - \frac{\eta^{*3}}{3}\right], \quad \omega = \frac{3}{e^2\xi}\left[1 - 2\eta^*\right]; \quad \text{for } \xi \to \infty,\ 0 \le \eta^* \le 1.$$

The numerical scheme employed to solve these equations was the line relaxation technique used in the earlier numerical paper and is standard (Fletcher, 1991). As mentioned in that article, the accuracy of the numerical solution is sensitive to the axial grid, and here the axial grid was chosen so as to capture fine details where necessary, for example, near the surface $z = L$. The smallest grid sizes used were $\Delta\chi = 0.00238$, $\Delta\eta = 0.0125$. This geometry presents a point of discontinuity for the vorticity at the sharp corner ($r = R$, $z = 0$), which was handled in the manner recommended by Roache (1972) and is described in the earlier article. Convergence of the stream function and vorticity equation was examined by computing the equation residuals at each grid point and continuing the iterations until the mean square value over the entire computational domain was less than a maximum error tolerance of 10^{-6}. The number of iterations necessary for convergence increase rapidly as the problems become convection dominated. This is a weakness of the numerical scheme employed here and is not unexpected (Fletcher, 1991). Furthermore, a relaxation factor less than unity (typically ~ 0.5) was required for Reynolds numbers ~ 50 and higher in order to avoid numerical instabilities. The results to be presented were all calculated using a value of $\beta = 0.1$. Partial verification of the numerical results was achieved by comparing the axial velocity profile at $z = 0$, $u_\eta(\xi, 0)$ for $Re = 0$, $e = (1/4, 0)$ and for $Re = 50$, ($e = 1, 4$) with the earlier calculations and found to be indistinguishable. In addition, for some of the cases the solution was reproduced on a finer grid with a reduced error tolerance (10^{-7} or 10^{-8}) and no significant difference was noted.

Numerical Results

In this flow field the flow entering through the pipe varies on the scale of R, whereas the appropriate length scale in the radial flow region is L, hence as $e = L/R$ is varied, the effect of the plate surfaces in shaping the flow in the vicinity of the entrance region is modulated. At low values of $e \lesssim 1$, upstream flow development in the pipe due to axial vorticity diffusion is significant at all Reynolds numbers. Figure 2a depicts the axial velocity profile at the plane $z = 0$ for various values of Re and e. This plot conveys two important points regarding upstream flow development in the pipe. First, for $Re = 100$ and $e = 2$ the axial velocity profile at $z = 0$ is practically identical to the classic parabolic velocity distribution for flow in a pipe. Second, for small e less than unity the axial-velocity distribution at $z = 0$ is not parabolic even at large Re, for instance, the velocity profile for $Re = 200$, $e = 1/2$ is distinctly different from the parabolic distribution. The profile for $Re = 100$, $e = 1/2$ is virtually identical to that for $Re = 200$, $e = 1/2$, and so the former profile is not shown in Figure 2a. Increasing Re further will have no effect on the axial-velocity profile at $z = 0$, since vorticity generation on the surface $z = L$ also increases with Re, and so the balance between the convective and diffusive terms in the vorticity transport equation, which determines the distortion in the velocity profile at $z = 0$, will not be affected. Another point to note is that for small e the precise shape of the axial velocity profile is strongly influenced by the value of e, for instance, the profile for $Re = 100$, $e = 1/4$ is substantially different from that for $Re = 100$, $e = 1/2$ (which is not shown but is virtually identical to the profile for $Re = 200$, $e = 1/2$).

Figure 2b shows a plot of the center-line axial velocity at the entrance plane $z = 0$, $u_\eta(0,0)$, as a function of the aspect ratio for aspect ratios varying over an order of magnitude from 1/4 to 6, and for various Reynolds numbers from 0 to 200. It is evident from this figure that upstream flow development becomes independent of the aspect ratio beyond $e \sim 2$ for each Reynolds number analyzed. For $Re = 0$, the limiting value matches the result for creeping flow through an orifice into an infinite half-space (Dagan et al., 1982) that represents the limit $e \to \infty$. Thus, an aspect ratio of ~ 2 appears to be a limiting value for upstream flow development at both low and

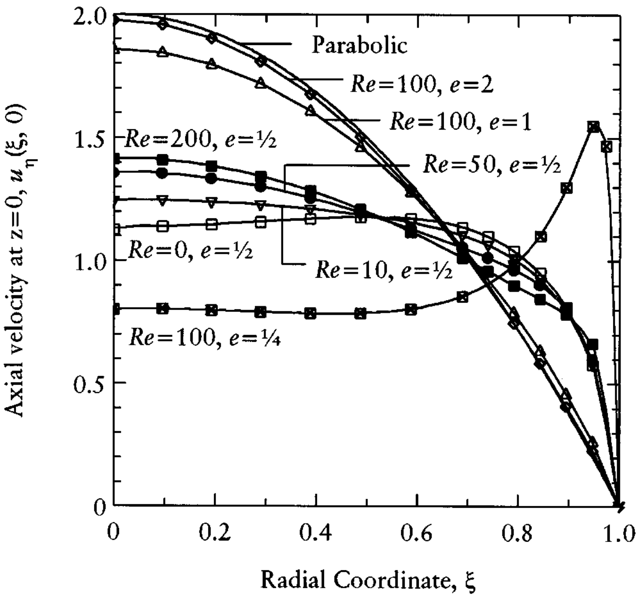

Figure 2a. Axial-velocity profiles at $z = 0$, $u_\eta(\xi,0)$, for the Reynolds number and aspect ratio.

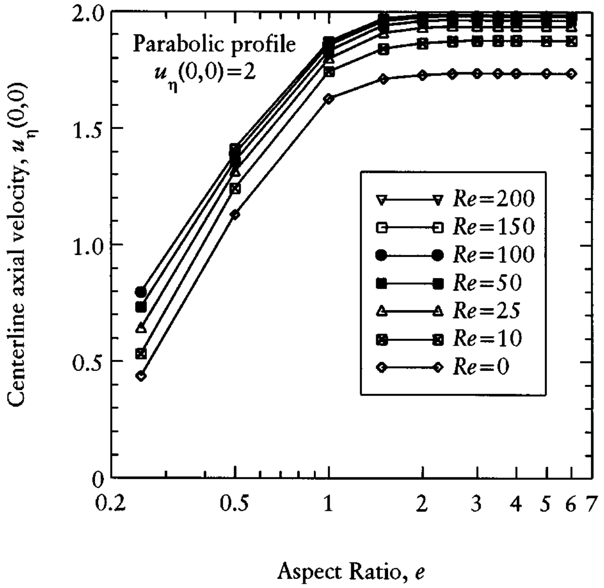

Figure 2b. Development of the centerline axial velocity $u_\eta(0,0)$ as a function of the aspect ratio for Reynolds numbers.

nonzero Reynolds numbers. This is similar to what is generally accepted regarding the flow features in the Newtonian sudden contraction geometry (Boger, 1987), where the limiting geometrical ratio is found to be 4. Based on the axial-velocity profiles depicted in Figure 2a and the limiting values of $u_\eta(0,0)$ in Figure 2b, we conclude that for $Re \geq \sim 100$ and $e > 2$, imposition of the parabolic axial velocity profile at $z = 0$ should introduce negligible error in calculating the developing velocity profile for $z > 0$. While this is equivalent to applying the parabolic boundary layer form of the equation of motion to the flow in the pipe, clearly a similar approximation of the equation of motion cannot apply in the region $z > 0$ due to the elongational character of the radial flow field.

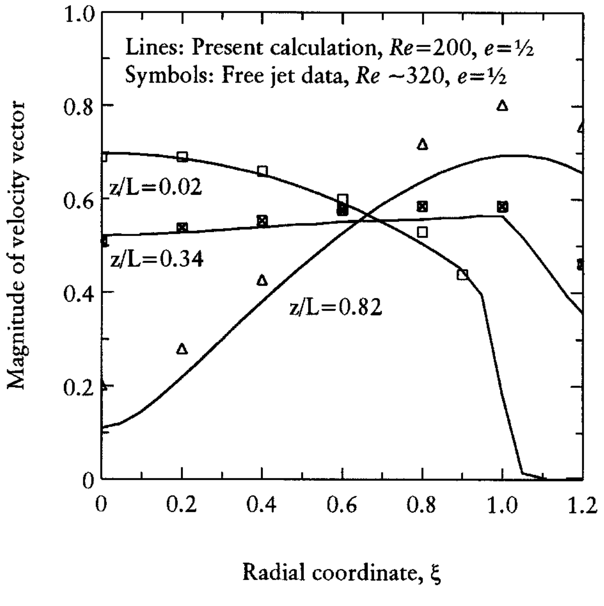

Figure 2c. Our calculations vs. the free jet data of Scholtz and Trass (1970) for $e = 1/2$.

In summary, the foregoing results show that when the approaching flow in the pipe is fully developed, the axial velocity distribution at $z = 0$ can always be taken to be parabolic for $Re \geq \sim 100$ and $e > 2$. On the other hand, for $e \lesssim 1$ the axial velocity profile at $z = 0$ will not be parabolic even at large values of Re, and the precise shape of the axial velocity profile will then depend strongly on the value of e. Fortunately, published analyses of confined laminar impinging-jet heat transfer have considered situations for which $e \gtrsim \sim 2$, where, as noted earlier, the imposition of a parabolic axial velocity profile at $z = 0$ is reasonable at high Re ($\geq \sim 100$). However, in view of our conclusion regarding flow development at $z = 0$ for $e \lesssim 1$, it should be apparent that the imposition of a parabolic axial velocity profile at $z = 0$ for low e is questionable regardless of the value of Re. While the importance of the precise shape of the axial velocity profile at $z = 0$ on the magnitude of the local Nusselt number on the surface $z = L$ for small $e \lesssim 1$ does not appear to have received attention, it seems clear that a proper analysis of this effect must employ the exact axial velocity profile at $z = 0$, since the shape of the profile depends strongly on e for $e \lesssim 1$. Experimental measurements of the dependence of the stagnation-point Nusselt number on aspect ratio in confined laminar impinging jets also have focused on large values of e, typically $e \gtrsim 2$, two recent articles being those of Lin et al. (1997) and Ma et al. (1997).

Finally, we note that Scholtz and Trass (1970) presented some experimental velocity profile measurements for a free axisymmetric laminar jet impinging on a flat surface at a small aspect ratio, $e = 0.5$. Although their flow configuration is not exactly similar to that studied here due to the absence of the confining plate at $z = 0$, we expect that their velocity distribution within the region $0 \leq r \leq R$ should be comparable to our calculations. They studied flows with Re in the range 320 to 883 and measured the velocity distribution at various axial distances from the impinging plane. Their data show a negligible influence of Re on the velocity distribution within $0 \leq r \leq R$ at each of the three axial positions at which measurements were taken. Figure 2c compares our calculated values of the magnitude of the velocity vector for $Re = 200$ (lines) with their experimental data ($Re \sim 320$, symbols) taken at three different axial locations z/L measured from the plane $z = 0$. In this plot the magnitude of the velocity vector is scaled with the maximum value for the parabolic profile. Our calculated curves for $z/L = 0.02$ and 0.34, that is, at locations away from the surface of the impinging plate at $z = L$, are in excellent agreement with the data over the entire range $0 \leq r \leq R$. This comparison reinforces our earlier comment regarding the inapplicability of the parabolic distribution for the axial velocity at $z = 0$ for small $e \lesssim 1$ regardless of the value of Re. Figure 2c also shows that when $z/L = 0.82$, which is close to the impinging surface, the magnitude of the computed velocity vector is uniformly smaller than the experimental measurement since the value of Re is lower for the calculated profile. At this axial location close to the impinging plane, the velocity field is not invariant with Re at $Re \sim 200$. Overall, this comparison with data is encouraging and provides

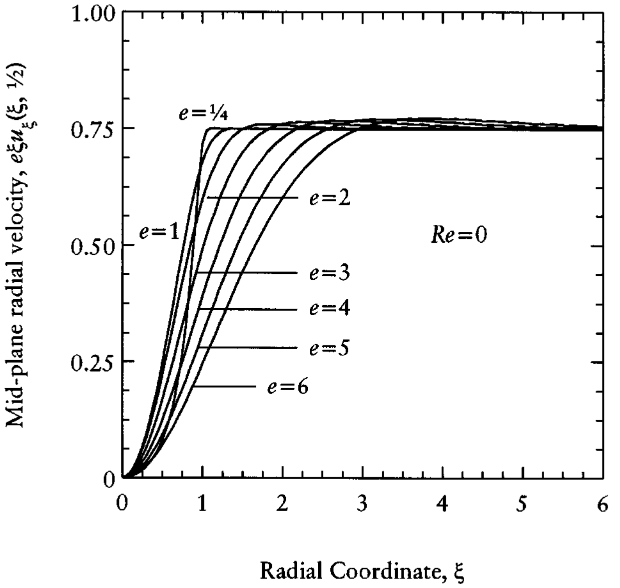

Figure 3. Development of the normalized midplane radial velocity for various aspect ratios at $Re = 0$.

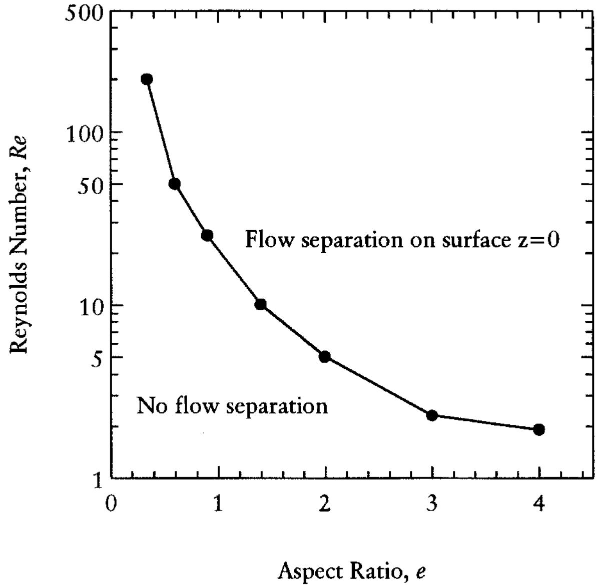

Figure 4. Demarcation of the $Re-e$ plane corresponding to flow separation on the surface $z = 0$.

some measure of the accuracy of the present numerical computations.

No flow separation near the sharp corner ($r = R$, $z = 0$) is seen at low Reynolds numbers for the entire range of aspect ratios investigated, and as seen in Figure 3, which plots the normalized midplane radial velocity component $[e\xi u_\xi(\xi, 1/2)]$, the midplane radial velocity increases monotonically with radial distance except for a small but slowly decaying overshoot prior to assuming the fully developed value of 3/4. The radial flow adjusts to the fully developed radial velocity profile between the circular plates within an entrance length Le (made dimensionless with R), which increases with the aspect ratio, and due to the overshoot in the profile, Le is defined here as the value of r/R at which the midplane radial velocity is at 1% above its fully developed value during its final asymptotic approach. As observed previously (Chatterjee, 1993), the entrance length in the creeping-flow limit should scale as $O(e)$ for large e, since the eigenfunctions describing the entrance disturbances decay on the scale of L, and not R. The present computations confirm this behavior and furnish the quantitative estimate for this linear scaling, which is given in Table 1.

The principal feature of flow development at nonzero Reynolds numbers is the occurrence of flow separation on the surface of the bottom plate ($z = 0$) near the sharp corner ($r = R$, $z = 0$). The flow subsequently reattaches downstream, and representative stream function plots depicting the primary clockwise vortex that characterizes the separated region are shown in the earlier numerical article, and will not be repeated here. Figure 4 presents a plot demarcating the region in the $Re-e$ plane, where flow separation is expected

Table 1. Radial Entrance Length (Le)* as a Function of Re and Aspect Ratio

Aspect Ratio, e,	Le ($Re = 0$)	Le ($Re = 10$)	Le ($Re = 25$)	Le ($Re = 50$)	Le ($Re = 100$)	Le ($Re = 150$)	Le ($Re = 200$)
0.25	1.05	1.05	1.27	1.54	2.47	—	—
0.5	1.11	1.11	1.71	2.17	3.43	—	4.87
1.0	1.27	1.65	2.41	3.36	4.87	6.02	6.92
1.5	1.38	2.17	3.03	4.19	6.02	7.31	8.46
2.0	1.94	2.65	3.63	4.87	6.92	8.46	9.76
2.5	2.41	3.10	4.34	5.67	7.82	9.51	10.97
3.0	2.84	3.56	4.95	6.37	8.46	10.41	12.02
3.5	3.30	4.05	5.59	7.12	9.27	11.25	12.8
4.0	3.77	4.56	6.19	7.92	10.02	12.02	13.9
5.0	4.64	5.59	7.51	9.39	11.70	13.58	15.6
6.0	5.51	6.55	8.80	10.97	13.37	15.20	17.1
α_0**	2.4	3.1	4.3	5.65	7.75	9.6	11.2
α_1**	0.89	0.99	1.27	1.52	1.6	1.61	1.7

*Le has been made dimensionless with R.

**Values of α_0, α_1 correspond to the linear scaling (Figure 6a), $Le = \alpha_0 + \alpha_1(e - 2.5)$ for large e.

to occur. This plot for the critical Reynolds number as a function of the aspect ratio was constructed by extrapolating the vortex length dependence on aspect ratio to zero at each Reynolds number. It conveys two important aspects of flow development in this radial entrance geometry: one, that separation occurs at very small Reynolds numbers when the aspect ratio is sufficiently large; and two, that small aspect ratios tend to suppress separation very readily even at reasonably large Reynolds numbers.

Thus, for a constant pipe radius, the flow separates more easily (at a smaller flow rate or a smaller value of *Re*), as the circular plates are placed farther apart. The features just noted are not unexpected, being due to the dominance of axial vorticity diffusion at low aspect ratios, which suppresses vorticity abstraction (Lighthill, 1988) at the surface $z = 0$, and thus prevents flow separation. However, they are in contrast to the situation encountered in radial source flow (Raal, 1978), which is the axisymmetric analog of entrance flow between parallel plates. In radial source flow, fluid enters the channel between the circular plates from a line source at $r = 0$. The flow domain is defined by a single length scale, the distance between the circular plates, and flow separation on the plate surfaces (both plates, since this configuration is symmetric about the midplane between the circular plates) is initiated at a fixed value of *Re* (based on this length scale) ~ 64. In the latter situation for a given rate of flow, since an increase in the distance between the plates results in a smaller Reynolds number, flow separation is suppressed when this distance is sufficiently large. So the essential difference between the two entrance geometries is that the presence of competing length scales (L/R) coupled with the change in flow direction enables flow separation at very small Reynolds numbers in the present entrance configuration.

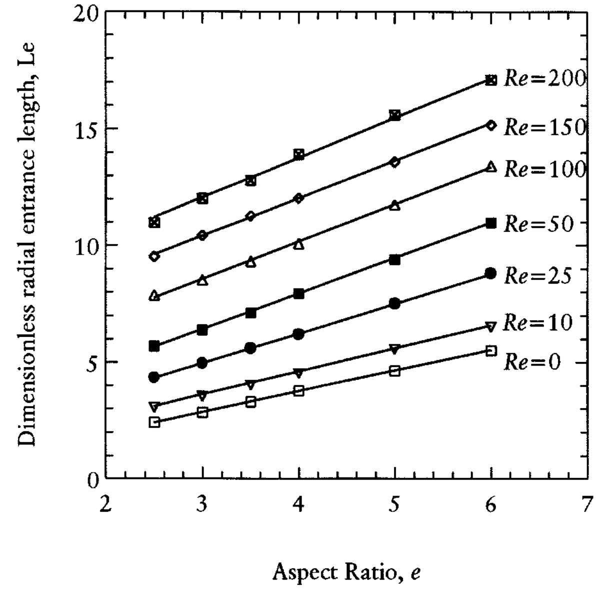

Figure 6a. Dimensionless radial entrance length *Le* as a function of the aspect ratio for various Reynolds numbers.

Figure 5 depicts the normalized midplane radial velocity component $[e\xi u_\xi(\xi, 1/2)]$ for $Re = 100$ at various aspect ratios. This plot shows the occurrence of flow separation for $e \geq 1$ leading to the region of negative radial velocity, and indicates that the primary clockwise vortex is large enough even at the relatively low value of $e = 2$ to span half the distance between the circular plates. The decay of entrance disturbances and the assumption of the fully developed radial velocity profile occurs over longer radial distances as the aspect ratio increases. And as shown in Figure 6a, the entrance length *Le* (made dimensionless with *R*) at nonzero Reynolds numbers also scales as $O(e)$, $Le \sim \alpha_0 + \alpha_1(e - 2.5)$, as e becomes large $(e > 2)$. Values of α_0 and α_1 for various

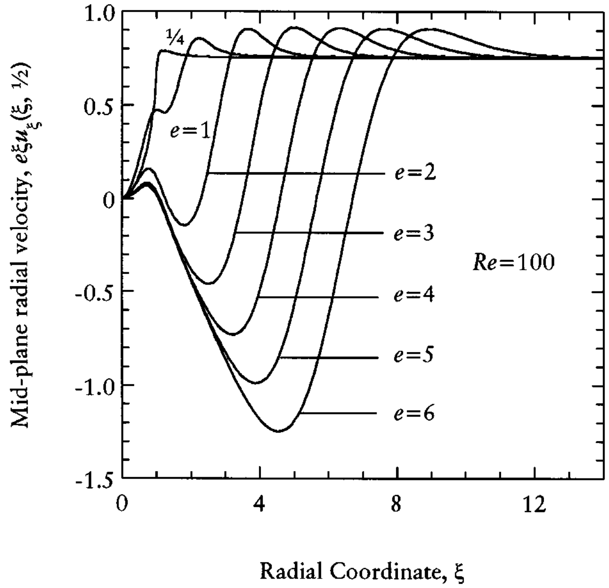

Figure 5. Development of the normalized midplane radial velocity for various aspect ratios at *Re* = 100.

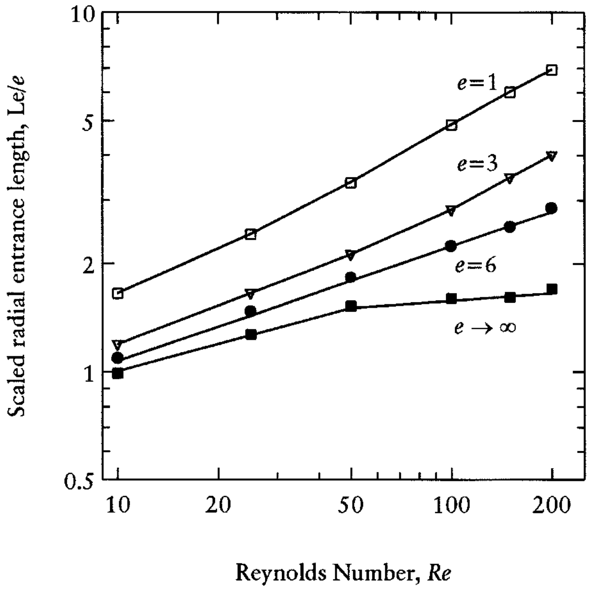

Figure 6b. Dimensionless scaled entrance length *Le*/*e* as a function of the Reynolds number.

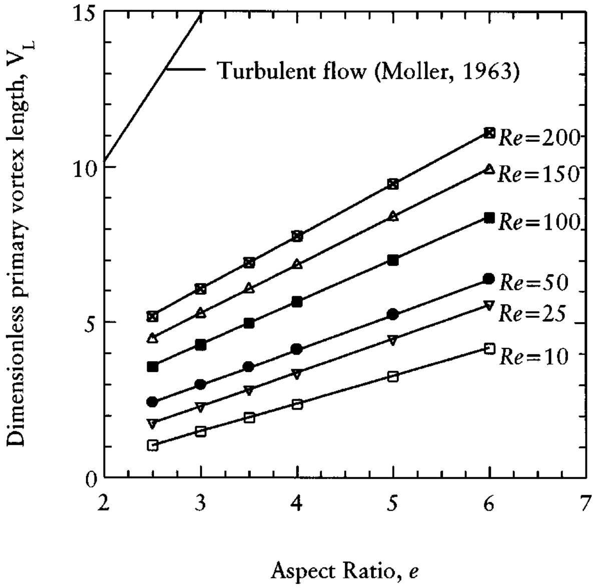

Figure 7a. Dimensionless vortex length V_L as a function of the aspect ratio for various Reynolds numbers.

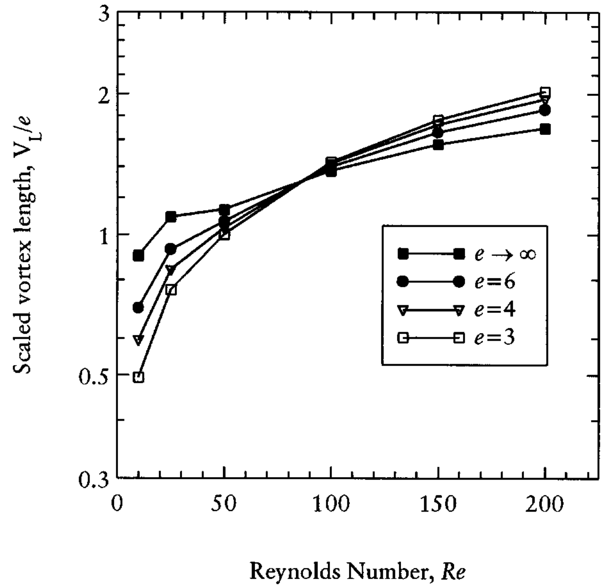

Figure 7b. Dimensionless scaled vortex length V_L/e as a function of the Reynolds number.

Reynolds numbers are tabulated in Table 1. The variation of the radial entrance length as a function of the Reynolds number is shown in Figure 6b, which plots the scaled entrance length Le/e vs. Re. This plot suggests that for Re away from zero ($Re \geq \sim 10$) and $e \gtrsim 3$, the behavior may be represented by cRe^m, where $m \sim 1/3$ and c is a very weak function of e, with $c \sim 0.51$ at $e = 6$. At very large values of e, however, the dependence of Le/e on Re vanishes as the Reynolds number is increased (beyond $Re \gtrsim 100$) as seen from the bottommost curve, which plots the values of α_1, the extrapolation to large e being reasonable provided the steady flow remains stable and laminar in this limit. Based on this, it may be conjectured that as Re is increased, the dependence on Re vanishes even for finite aspect ratios, but presumably this occurs at values of Re larger than ~ 100. Some indirect evidence in support of this statement is noted below. In the sudden contraction geometry $m = 1$ at high Reynolds numbers based on the boundary-layer equations, whereas here the dependence on Re is weaker, $m < 1$, a consequence of the change in flow direction in this entrance configuration, which hinders axial convection from transporting entrance disturbances to large radial distances downstream. In summary, then, for large aspect ratios and $Re \geq \sim 100$ the dimensional radial entrance length is given simply as $\alpha_1 L$, where α_1 is well approximated by $\alpha_1 \sim 1.6$–1.7. Finally, we also point out that for Reynolds numbers between 0 and ~ 10, the entrance length values differ only by ~ 10–20% (Table 1), and so the effect of inertia in this range is not very significant.

Figure 7a displays, as a function of the aspect ratio and for different Reynolds numbers, the dimensionless vortex length V_L (scaled with R) of the primary clockwise vortex whose presence signifies flow separation near the sharp corner, V_L being computed simply as the difference between the radial coordinates of the reattachment and separation points, as sketched in Figure 1. Table 2 also summarizes the dimensionless vortex size V_S (scaled with R), which is defined as the Cartesian distance of the vortex center from the separation point (typically within a grid point of the sharp corner $r = R$, $z = 0$) in the $\xi - \eta$ plane. From Figure 7a it is apparent that for each Reynolds number the vortex length V_L scales linearly with the aspect ratio for large e ($e \gtrsim 2$), $V_L = \gamma_0 + \gamma_1(e - 2.5)$. A similar linear scaling also applies to the vortex size, and the coefficients γ_0 and γ_1 are listed in Table 2 for both V_L and V_S. It is interesting to note that experimental data taken by Moller (1963) at very large Reynolds numbers also show a linear behavior with the aspect ratio e for the coordinate of the reattachment point, which is effectively equal to $V_L + 1$ since flow separation occurs very close to $r = R$. His experimental asymptote plotted in Figure 7a suggests that V_L scales as $\sim 5e$ under conditions where the flow is expected to be turbulent. Figure 7b depicts the variation in the scaled vortex length, V_L/e, as a function of the Reynolds number. In this plot the curve for $e \to \infty$ was constructed by plotting the values of γ_1 from Table 2a, and as before, the extrapolation to large e is reasonable provided the steady flow continues to remain stable and laminar in this limit. Figure 7b indicates that for each aspect ratio considered, V_L/e shows a relatively weak dependence on Re and appears to possess a limiting value close to ~ 2, the exact limiting value decreasing weakly (e^{-1}) as the aspect ratio is increased. This provides some indirect evidence that the scaled radial entrance length plotted in Figure 6b should also, as conjectured earlier, become independent of Re at large Reynolds numbers for each aspect ratio. Moller's (1963) data, again although not directly comparable to the present situation owing to the turbulent flow conditions in his experiment, also show a clear approach to an asymptotic value for the scaled vortex length V_L/e, his data being taken for aspect ratios less than unity. For the values of aspect ratio considered, his data indicate a limiting value close

Table 2a. Primary Vortex Size $(V_S)^*$ and Length $(V_L)^*$ as a Function of Re and Aspect Ratio

Aspect Ratio, e	$Re = 10$		$Re = 25$		$Re = 50$		$Re = 100$		$Re = 150$		$Re = 200$	
	V_S	V_L	V_S	V_L	V_S	V_L	V_S	V_L	V_S	V_L	V_S	V_L
0.5	—	—	—	—	—	—	—	—	—	—	0.25	0.53
1.0	—	—	—	—	0.28	0.56	0.64	1.19	0.97	1.72	1.31	2.15
1.5	—	—	0.38	0.68	0.69	1.23	1.16	2.06	1.64	2.72	2.16	3.28
2.0	0.24	0.56	0.74	1.22	1.12	1.84	1.68	2.83	2.28	3.62	2.89	4.26
2.5	0.56	1.03	1.09	1.76	1.54	2.43	2.16	3.56	2.88	4.47	3.59	5.18
3.0	0.79	1.48	1.49	2.28	1.94	2.99	2.67	4.27	3.46	5.28	4.20	6.07
3.5	1.03	1.92	1.83	2.82	2.36	3.56	3.12	4.97	4.00	6.08	4.84	6.94
4.0	1.28	2.37	2.19	3.36	2.77	4.13	3.59	5.66	4.55	6.86	5.42	7.79
5.0	1.73	3.27	2.93	4.45	3.57	5.26	4.47	7.02	5.57	8.40	6.59	9.46
6.0	2.20	4.17	3.62	5.56	4.41	6.39	5.40	8.37	6.60	9.93	7.75	11.1
γ_0^{**}	0.56	1.03	1.11	1.74	1.54	2.4	2.19	3.6	3	4.5	3.62	5.22
γ_1^{**}	0.47	0.9	0.72	1.09	0.82	1.13	0.92	1.37	1.03	1.56	1.19	1.69

Table 2b. Primary Vortex Circulation $(C)^\dagger$ as a Function of Re and Aspect Ratio

Aspect Ratio, e	$Re = 10$ $C \times 10^2$	$Re = 25$ $C \times 10^2$	$Re = 50$ $C \times 10^2$	$Re = 100$ $C \times 10^2$	$Re = 150$ $C \times 10^2$	$Re = 200$ $C \times 10^2$
0.5	—	—	—	—	—	0.53
1.0	—	—	4.03	30.1	54.0	75.2
1.5	—	6.28	41.01	88.2	119.0	144.5
2.0	0.49	27.83	82.80	135.9	168.5	195.5
2.5	4.02	55.67	121.9	176.8	211.0	238.8
3.0	8.96	82.10	156.6	214.1	249.4	277.2
3.5	14.52	107.3	189.1	250.0	285.1	312.5
4.0	19.97	131.0	219.8	283.5	319.5	346.8
5.0	29.76	173.9	280.7	349.3	385.8	412.2
6.0	37.54	212.3	336.3	417.0	456.4	484.6

[*] Vortex size and length have been made dimensionless with R.

[**] Values of γ_0, γ_1 correspond to the linear scaling (Figure 7a), V_S, $V_L = \gamma_0 + \gamma_1(e - 2.5)$ for large e.

[†] Circulation has been made dimensionless with UR.

to ~ 6, the precise value decreasing with the aspect ratio (just as in the present calculations) due to the linear scaling of V_L with e noted earlier.

It is instructive to compare the size of the primary vortex in the present case with that for radial source flow (Raal, 1978). The vortex lengths for the two cases are listed in Table 3. We have chosen $e = 1$ in order to define the Reynolds number using the distance between the circular plates, since this is the only length scale in radial source flow. The correspondence between our definition of the Reynolds number (Re) and that for radial source flow (Re_{RSF}) is $Re = 4 Re_{RSF}$ (Raal, 1978). From Table 3 we note that our vortex length for $Re = 200$, which is equivalent to $Re_{RSF} = 50$, is already larger than that for radial source flow at $Re_{RSF} = 100$. So we conclude that for moderate values of $Re \sim 200-400$ the vortex size is considerably larger with the present entrance configuration. However, given the weak dependence of V_L/e on Re described in Figure 7b, it would appear that at higher values of Re this conclusion may not hold. Indeed, if we use Moller's (1963) data as a limiting value at high Re, for very large Re and $e = 1$, we obtain a value of $V_L/e \sim 5.5$, which is smaller than that for radial source flow at $Re_{RSF} = 300$, $Re = 1{,}200$ (Raal, 1978). Thus apart from the asymmetry about the midplane at $z = L/2$ in the present entrance configuration (for instance, the absence of a corresponding primary vortex on the surface $z = L$), the other features that are distinct vis-à-vis radial source flow are: the occurrence of flow separation on the surface $z = 0$ at very small nonzero Reynolds numbers, and the considerably weaker dependence of the primary vortex length on Re.

Table 3. Comparison of Dimensionless Vortex Lengths*

Reynolds Number $(Re^{**} = 4 Re_{RSF}{}^{\dagger})$		Radial Entrance Flow $e = 1$	Radial Source Flow (Raal, 1978)
$Re = 50$;	$Re_{RSF} = 12.5$	0.56	No flow separation
$Re = 100$;	$Re_{RSF} = 25$	1.18	No flow separation
$Re = 150$;	$Re_{RSF} = 37.5$	1.72	No flow separation
$Re = 200$;	$Re_{RSF} = 50$	2.15	No flow separation
$Re = 400$;	$Re_{RSF} = 100$	—	1.85

[*] The primary vortex length has been made dimensionless with L $(= R$, since $e = 1)$.

[**] Re: value of the Reynolds number in this work $(e = 1)$.

[†] Re_{RSF}: corresponding value of the Reynolds number for radial source flow (Raal, 1978).

It is also interesting to contrast the flow development features of the present axisymmetric configuration with the corresponding 2-D Cartesian geometry. While both geometries display flow separation near the sharp corner, it is expected that the elongational character of the radial flow field in the axisymmetric configuration will lead to differences in subsequent flow development between the two configurations. The 2-D Cartesian situation has been considered in some detail

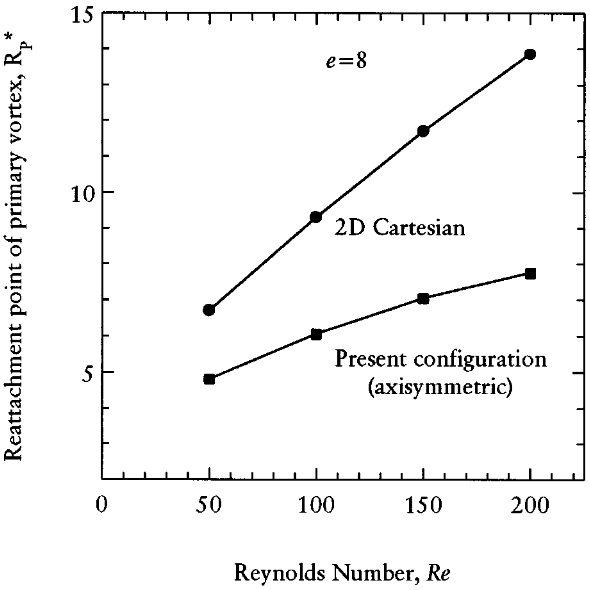

Figure 8a. Comparison of R_P for the present axisymmetric configuration and the corresponding 2-D Cartesian geometry for various Reynolds numbers.

R_p has been scaled with $2R$.

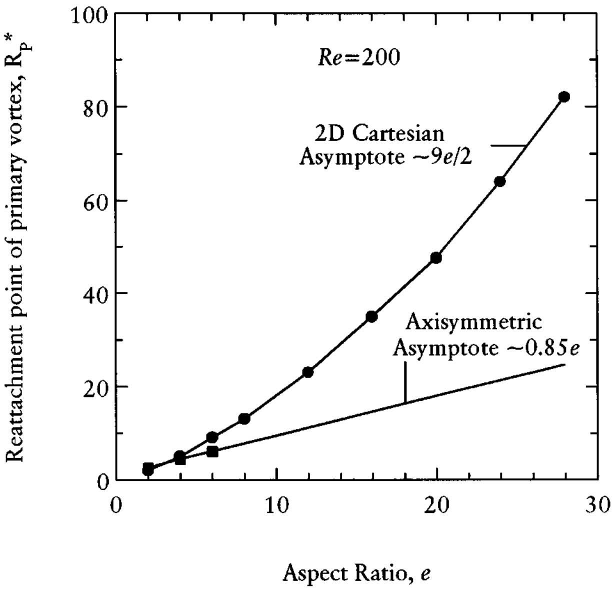

Figure 8b. Comparison of R_P for the present axisymmetric configuration and the corresponding 2-D Cartesian geometry as a function of the aspect ratio.

R_p has been scaled with $2R$.

by Law and Masliyah (1984), and limited results are also contained in Al-Sanea (1992) and in Schafer et al. (1992). In all these studies a specific form (either flat or parabolic) for the axial velocity distribution was imposed at $z = 0$ and computation was restricted to the region $z > 0$. One of the most significant differences in flow separation behavior between the two geometries relates to flow reattachment on the surface $z = 0$, the reattachment point occurring considerably earlier in the present axisymmetric configuration. This is demonstrated in Figure 8a, which displays a comparison of the coordinate of the reattachment point R_P of the primary vortex as a function of Re. Since the separation point of the primary vortex effectively is at $r = R$ for high Re (~ 100) and large e ($\gtrsim 2$), R_P is given simply as $R_P = V_L + 1$ in dimensionless terms, where V_L is the vortex length summarized in Table 2a.

The results in Figure 8a are for $e = 8$, and our data have been calculated based on the linear scaling established in Figure 7a. Note that the aspect ratio "Z" in Al-Sanea (1992) is defined on the basis of the jet width, and is therefore equivalent to half our value, which is based on the pipe radius, and correspondingly, for a proper comparison our values of R_P in Figure 8a have been divided by 2 to reflect the scaling on the basis of the pipe diameter $2R$. The plot in Figure 8a shows that the primary clockwise vortex extends significantly further downstream in the 2-D rectangular geometry compared to the present axisymmetric situation where flow reattachment occurs relatively early. This early reattachment is a consequence of the decay of inertia with radius which enables axial diffusion to restore the vorticity on the lower plate surface $z = 0$ to a positive value at a relatively short radial distance from the axis of symmetry. In consequence of the longer vortex length in the Cartesian geometry, we also expect the entrance length in the Cartesian case to be much larger than that in the present axisymmetric configuration. Another difference between the two geometries is in the dependence of the location of the reattachment point R_P (or equivalently the vortex length V_L) on the aspect ratio e at a fixed Reynolds number; this is depicted in Figure 8b. In the present case asymptotic dependence of R_P (or V_L) on e is assumed relatively quickly, for $e \gtrsim 2$, and the dependence for large e is quite weak, R_P, $V_L \sim 0.85e$, at $Re = 200$ from the results summarized in Table 2a. (Note: R_P, V_L are scaled with $2R$ in Figure 8b.) As seen in Figure 8b, however, Al-Sanea (1992) computes that for $Re = 200$ in the 2-D Cartesian geometry, asymptotic behavior is achieved only beyond $e \sim 24$ ($Z \sim 12$) and the quantitative dependence on aspect ratio is stronger, with R_P, $V_L \sim 9e/2$ (R_P, $V_L \sim 9Z$).

The strength of the primary vortex can be measured by computing the circulation around the streamline $\psi = 0$ that bounds the separation region. This quantity is computed using the expression $C = \int_A \omega \, dA$, where A is the area enclosed by the streamline $\psi = 0$. Since this area (made dimensionless with R^2) scales as $\sim e^2$ for large e, in Figure 9 we have plotted C/e^2 as a function of e for various Reynolds numbers. We observe that the circulation increases initially due to the faster than $O(e^2)$ growth of the area occupied by the vortex, but beyond the point where this area assumes its asymptotic form ($\sim e^2$), the circulation decays roughly as $\sim e^{-1}$ for the larger values of Re ($\geq \sim 50$), the asymptote at $Re = 200$ being given approximately by $\sim 0.8/e$. For large values of Re and e the variation of vorticity within the vortex is effectively confined to a layer adjacent to the boundary of the vortex where the flow inside the vortex matches the external flow (near $r \approx R$), the magnitude of the vorticity in the bulk of the vortex being uniformly small. The thickness of this layer and the vorticity within it are essentially independent of both Re

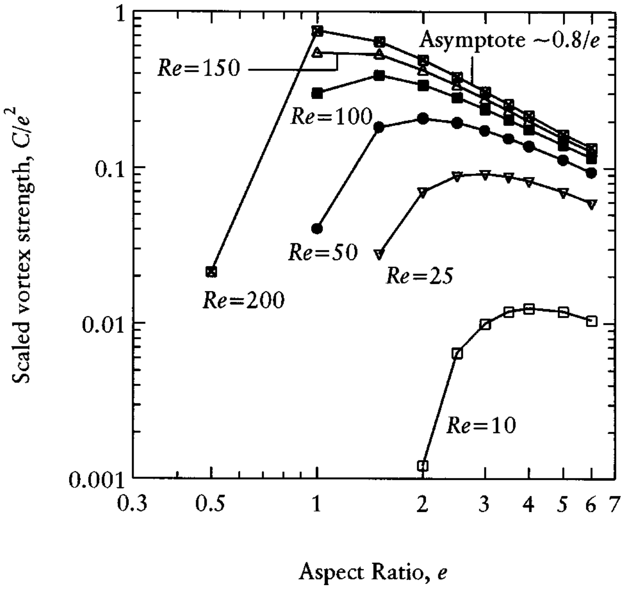

Figure 9. Dimensionless strength of the primary vortex C/e^2 as a function of the aspect ratio for various Reynolds numbers.

and e, being determined by the incoming pipe flow. Figure 9 also shows that for $e \gtrsim 2$ the circulation is a weak function of Re, essentially becoming independent of the Reynolds number for $Re \gtrsim 100$.

One of the important quantities of interest in this flow field is the shear-stress profile on the surfaces of the circular plates at $z = 0$, L. The earlier analytical work (Chatterjee, 1993) presented the behavior in the creeping-flow limit.

Figure 10a depicts the shear-stress (made dimensionless with $\mu U/R$) profiles at $z = 0$ for different aspect ratios at $Re = 50$, 200. For $e = 1$ we note the change in the sign of the shear stress across the reattachment point and observe that the profiles rapidly merge with the fully developed creeping-flow profile beyond the reattachment point. Thus the stress on the bottom plate surface is quite low at large aspect ratios, and for low aspect ratios it is close to the creeping-flow value except for the relatively small separation region. Figure 10b depicts the shear stress on the surface $z = L$. Here we note that the shear stress increases rapidly beyond the stagnation point as the fluid quickly acquires a nonzero radial velocity, but this increase is arrested sharply once viscosity begins to retard the radial flow away from the surface $z = L$. We also note that for both Reynolds numbers, the decay in the shear-stress profile some distance beyond the peak appears to acquire a similar form independent of the aspect ratio for $e = 5$, 6. It is instructive to examine to what extent boundary-layer arguments can be used at high Reynolds numbers to model the flow in the vicinity of the surface $z = L$. It would appear that at large Re some features of the flow in this region can mimic the radial flow due to an axisymmetric jet impinging on a plane wall. This latter problem has been analyzed by Watson (1964), who employed boundary-layer arguments to derive a similarity solution that is expected to apply at distances far away from the center of the jet. A very readable account of Watson's analysis is given in Middleman (1995). This analysis permits an easy calculation of the shear stress on the surface of the plate $z = L$, which can be compared with our numerical computations. Watson's result for the shear stress is given by eq. P5.4-3 of Middleman (1995); however, this expression appears to contain an error—the numerical coefficient 0.141 should be replaced by 0.124π. Thus, Watson's expression for radial distribution of the dimensionless shear stress (scaled with $\mu U/R$) on the surface $z = L$ is given by

$$\frac{\tau_{\eta^*=1}}{Re} = \frac{1}{2}\,\frac{0.124\pi Re\xi}{\left[\xi^3 + 0.286 Re\right]^2}.$$

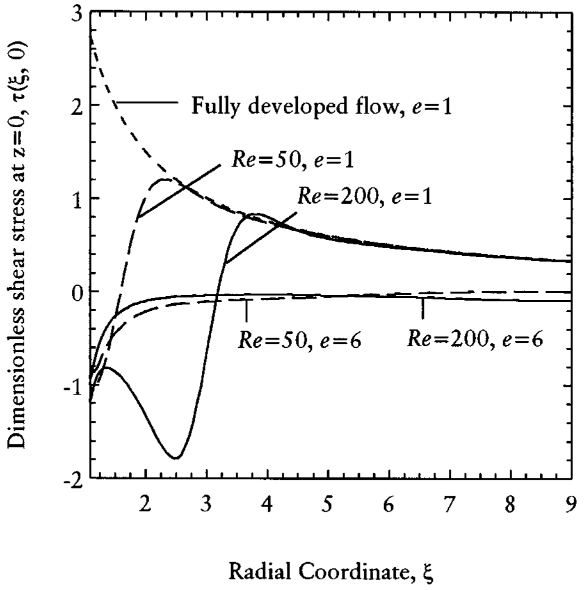

Figure 10a. Dimensionless shear stress profile on the surface $z = 0$ at $Re = 50$, 200.

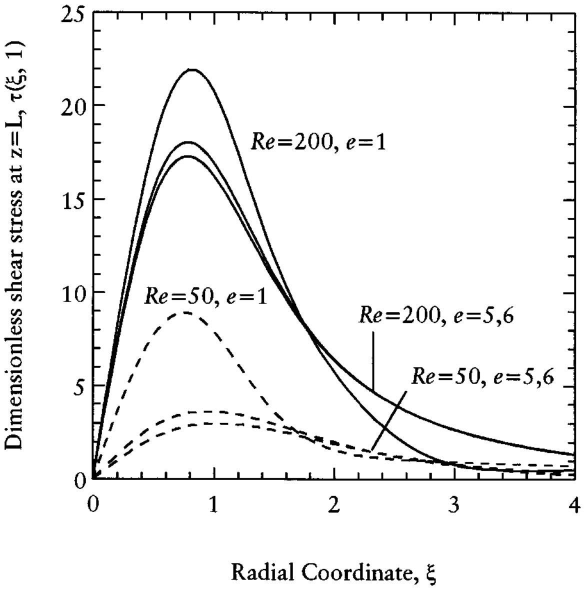

Figure 10b. Dimensionless shear stress profile on the surface $z = L$ at $Re = 50$, 200.

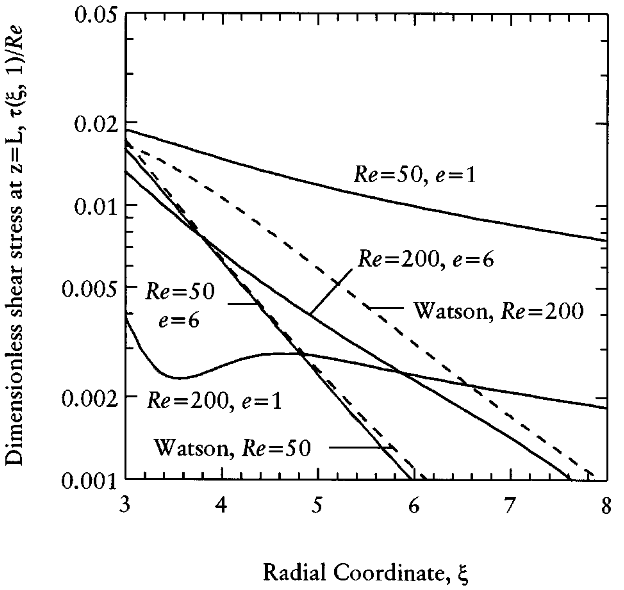

Figure 11. Comparison of the decay in the shear-stress profile on the surface $z = L$ with Watson's boundary-layer solution for $Re = 50$, 200 and $e = 1$, 6.

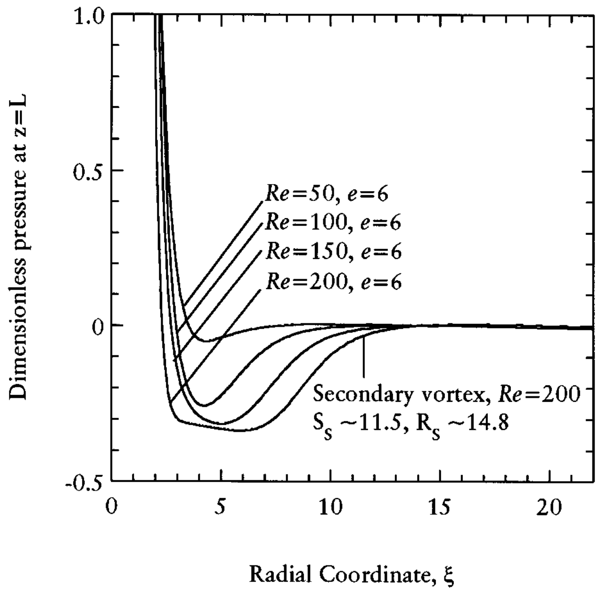

Figure 12. Pressure distribution on the surface $z = L$ for various Reynolds numbers at $e = 6$.

Figure 11 displays the comparison between our calculations and the preceding expression at aspect ratios $e = 1$, 6 for $Re = 50$ and $Re = 200$. This figure indicates that for both Reynolds numbers, at $e = 6$ the form of the decay in the shear-stress profile at radial distances where the flow becomes independent of the details of the jet (beyond the peak in Watson's profile), and prior to its assuming the fully developed profile, is surprisingly well represented by Watson's solution. The numerical agreement is better at $Re = 50$, which presumably is just a fortuitous circumstance. On the other hand, for both Reynolds numbers our calculation for $e = 1$ has a slope that shows considerable deviation from Watson's result, indicating that at low aspect ratios the flow near the surface $z = L$ interacts strongly with the flow away from it, thus leading to an early assumption of the more modest ξ^{-1} rate of decay characteristic of fully developed creeping flow. In other words, even at relatively high Reynolds numbers (~ 200) the assumption of a growing boundary layer on the surface $z = L$ that is inherent in Watson's analysis is not applicable for aspect ratios $e \leq \sim 1$.

Figure 12 depicts the pressure profile (made dimensionless with $\mu U/R$) on the surface of the circular plate at $z = L$ for $Re = 50$, 100, 150, and 200, and $e = 6$. The plot shows that the pressure decays rapidly from the stagnation point in each case, and we note a region of positive pressure gradient prior to the subsequent decay in the pressure profile as the flow begins to acquire its fully developed form. This adverse pressure gradient arises in the region where the main flow expands to fill the radial channel as it goes past the primary vortex, and if large enough, will result in flow separation on the surface $z = L$. Figure 12 indicates that the positive pressure gradient increases as a function of Re at a fixed aspect ratio, and our computations signal the occurrence of such flow separation only at $Re = 200$, for $e \geq 2.5$. Figure 13 plots the coordinates of the separation and reattachment points of this secondary vortex and demonstrates that they correlate very well with the location of the reattachment point of the primary vortex, indeed scaling almost linearly with it over the entire range of e from 2.5 to 6. This secondary vortex, which has also been observed in the 2-D Cartesian configuration (Law and Masliyah, 1984; Schafer et al., 1992), is not a significant feature of the flow field at $Re = 200$. It occupies a small

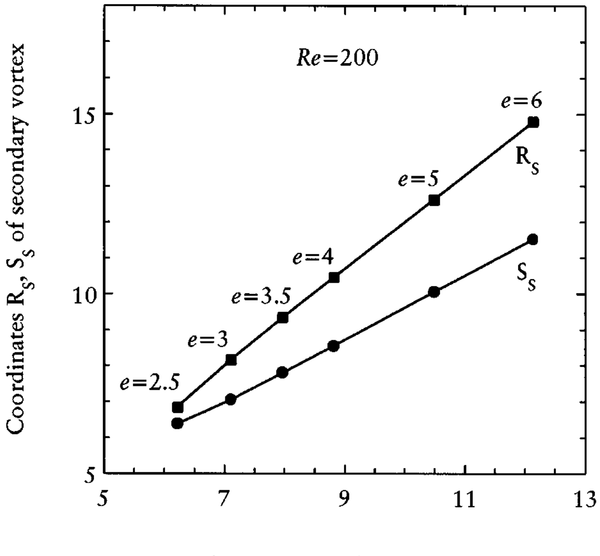

Figure 13. Dependence of the coordinates of the separation (S_S) and reattachment (R_S) points of the secondary vortex on the location of the reattachment point of the primary vortex R_P for $Re = 200$.

Table 4. Excess Pressure Loss $(\Delta P_e)^*$ as a Function of Re and Aspect Ratio

Aspect Ratio, e	ΔP_e $Re=0$	ΔP_e $Re=10$	ΔP_e $Re=25$	ΔP_e $Re=50$	ΔP_e $Re=100$	ΔP_e $Re=150$	ΔP_e $Re=200$
0.25	66.90	69.80	71.40	79.96	109.40	—	—
0.50	17.97	18.55	19.08	21.17	30.06	—	52.65
1.0	6.69	7.01	9.38	16.14	34.18	54.74	76.28
1.5	5.15	5.76	9.61	19.41	41.35	64.39	88.04
2.0	4.78	5.56	10.30	21.19	44.16	68.09	92.37
2.5	4.68	5.58	10.81	22.05	45.56	69.83	94.45
3.0	4.65	5.60	11.06	22.46	46.22	70.82	95.76
3.5	4.65	5.62	11.20	22.69	46.72	71.49	96.78
4.0	4.64	5.64	11.28	22.81	46.94	72.03	97.76
5.0	4.64	5.64	11.35	23.04	47.25	72.20	98.02
6.0	4.64	5.64	11.36	23.07	47.30	72.25	98.10

$^*\Delta P_e$ has been made dimensionless with $\mu U/R$. The kinetic energy change has been excluded from the value of ΔP_e.

region of the domain, extending vertically only to $\sim 15\%$ of the plate-to-plate distance L for $e=6$, and with a circulation within it that is more than ~ 100 times weaker than that of the primary vortex after normalizing for the difference in the areas of the respective vortices. We also note that since flow reattachment on the surface $z=0$ occurs considerably later in the 2-D Cartesian geometry, as seen in Figures 8a and 8b, and because the location of the second vortex correlates with R_P, we expect the secondary vortex to appear further downstream in the Cartesian situation. For $Re=200$, $e=8$ Law and Masliyah (1984) indicate that the vortex center of the secondary vortex occurs at ~ 30 half jet widths from the axis of symmetry. This is approximately twice the value we estimate for $Re=200$, $e=8$ by extrapolating the data in Figure 13 to $e=8$ through the use of the linear scaling in Table 2a.

For this radial entrance flow field we tabulate our results for the excess loss in pressure (made dimensionless with $\mu U/R$) in Table 4 for various values of Re and the aspect ratio. This quantity is conveniently calculated from the mechanical energy balance equation and is given in dimensionless form by

$$\Delta P_e = \frac{1}{\pi}\int_V \Phi\, dV - \left(\Delta P_{\text{pipe}}\right)^{fd} - \left(\Delta P_{\text{plates}}\right)^{fd},$$

where fd refers to fully developed flow, V is the volume of the entrance geometry, and Φ is the dimensionless viscous dissipation function. The excess pressure loss term thus excludes the kinetic-energy loss, which is simply $0.5Re$ for this entrance geometry. From Table 4 we note that the creeping-flow results are in good agreement with our earlier infinite series calculation (Chatterjee, 1993) for $e \geq \sim 1$. At nonzero Reynolds numbers the excess pressure loss initially decreases as a function of the aspect ratio just as in creeping flow, but this decay is arrested at the onset of flow separation on the surface $z=0$, beyond which the excess pressure loss increases due to the initial faster than $O(e^2)$ growth of the primary vortex, which rapidly displaces the main flow toward the surface $z=L$ and increases shear rates there. However, the excess pressure loss approaches its asymptotic value relatively quickly as the aspect ratio is increased beyond the point of incipient flow separation to $e \gtrsim 2$, where the flow structure has adopted its asymptotic form with the primary vortex area scaling as $\sim e^2$. At high aspect ratios and $Re \geq \sim 100$ the contribution to the total viscous dissipation from the primary vortex is small (a few percent), with excess viscous effects being effectively consigned to a “thin” layer external to the vortex, in this case adjacent to the surface $z=L$. This situation is somewhat reminiscent of the constant vorticity inviscid core model for steady flow with closed streamlines (Batchelor, 1967). At a given aspect ratio e the excess pressure loss increases with the Reynolds number, as seen from the data in Table 4. What is perhaps not so immediately apparent from Table 4 is that as Re and e are increased, beyond $Re \approx 50$ and $e \approx 3$, the dependence of the excess pressure loss on Re is linear with a slope of 0.5, this dependence arising because the pressure loss has been scaled with the viscous reference scale $\mu U/R$ and not the inertial scale ρU^2. Thus, for large Re and e the excess pressure loss excluding the kinetic energy change is given simply by $\Delta P_e \sim Re/2$.

Concluding Remarks

The developing laminar flow field in this radial entrance geometry has been analyzed for a range of aspect ratios e and the Reynolds numbers Re. The principal feature of the developing flow is the occurrence of flow separation on the surface $z=0$ at a critical value of Re that is quite small at large e, but increases sharply for $e \lesssim 1$, a consequence of the dominance of axial vorticity diffusion at small aspect ratios. The calculations highlight the importance of the aspect ratio, for small $e \lesssim 1$, in influencing upstream flow development at all values of Re, in suppressing flow separation on the surface $z=0$, and in invalidating the applicability of boundary-layer arguments to model the local flow near the surface $z=L$. They also show that as the aspect ratio is increased, the flow structure approaches an asymptotic form relatively rapidly, for $e \gtrsim 2$. The calculated velocity profiles in the “pre-impingement” region $(0 \leq r \leq R,\ 0 \leq z < L)$ compare very well with the experimental data of Scholtz and Trass (1970) taken at $e=0.5$, a value at which axial vorticity diffusion is significant and the axial velocity profile at $z=0$ is distorted significantly from the classical parabolic distribution. The present calculations, which cannot be directly compared with Moller’s (1963) data, nevertheless reproduce qualitatively some of the features of his experimental observations. At the same time, for $Re=200$, $e \geq 2.5$ our results indicate the existence of a small secondary vortex due to flow separation region on the surface $z = L$, a feature not observed in Moller's experiments conducted at much higher values of Re, but at aspect ratios $e < 1$, typically $e \ll 1$. The influence of the elongational character of the radial flow in this axisymmetric geometry has been clarified by comparing certain aspects of flow development with the corresponding 2-D Cartesian configuration. Finally, let us note that, based on the flow development results presented here, it would appear that the analysis of heat and mass-transport phenomena in this geometry, assuming fully developed radial creeping flow or minor variations of it (Camera-Roda et al., 1994), should be viewed with caution, particularly at high Re and $e > 1$. These approximate flow fields cannot capture the effects of the large primary vortex and the consequent asymmetry about the midplane $z = L/2$. Indeed, the very dissimilar behavior of the local dimensionless shear stress (equivalently the skin friction coefficient) along $z = 0$ and $z = L$ would suggest, on the basis of the transport analogies, that the local dimensionless heat/mass transfer coefficients will reflect this asymmetry. On the other hand, at radial distances far away from the axis of symmetry, for $r \gg R$, where the flow field begins to assume its fully developed form, calculations based on approximate creeping-flow type of velocity profiles possibly may be adequate.

Acknowledgment

The author is indebted to Stefania Za at the University of California Irvine for her assistance in providing access to some literature references not locally available.

Notation

$r =$ radial coordinate
$u =$ fluid velocity
$z =$ axial coordinate
$\alpha, \gamma =$ numerical coefficients in the asymptotic behavior of the entrance length and vortex length, vortex size
$\mu =$ fluid viscosity
$\rho =$ fluid density
$\tau =$ dimensionless shear stress (scaled with $\mu U/R$)

Superscripts, subscripts, and special symbols

$\chi =$ radial velocity component
$\Delta\xi, \Delta\chi =$ radial grid size
$\eta =$ axial velocity component
$\Delta\eta =$ axial grid size
$S_P =$ dimensionless radial coordinate of the separation point of the primary vortex (scaled with R)
$V_S =$ dimensionless vortex size of the primary vortex (scaled with R)

Literature Cited

Al-Sanea, S., "A Numerical Study of the Flow and Heat Transfer Characteristics of an Impinging Laminar Slot-Jet Including Crossflow Effects," *Int. J. Heat Mass Transfer*, **35**, 2501 (1992).

Batchelor, G. K., *An Introduction to Fluid Dynamics*, Cambridge Univ. Press, New York (1967).

Behnia, M., S. Parneix, Y. Shabany, and P. Durbin, "Numerical Study of Turbulent Heat Transfer in Confined and Unconfined Impinging Jets," *Int. J. Heat Fluid Flow*, **20**, 1 (1999).

Boger, D. V., "Viscoelastic Flows Through Contractions," *Annu. Rev. Fluid Mech.*, **19**, 157 (1987).

Camera-Roda, G., C. Boi, A. Saavedra, and G. C. Sarti, "Heat and Mass Transfer Boundary Layers in Radial Creeping Flow," *Int. J. Heat Mass Transfer*, **37**, 2145 (1994).

Chatterjee, A., and D. White, "Radial Entry Flow of a Newtonian Fluid," *J. Phys. D: Appl. Phys.*, **22**, 915 (1989).

Chatterjee, A., "An Infinite Series Solution for the Creeping Radial Entrance Flow of Newtonian Fluid," *AIChE J.*, **39**, 1563 (1993).

Chen, C.-P., "Contribution a l'Etude Experimentale de l'Ecoulement Radial d'un Fluide Visquex Incompressible Entre deux Disques Paralleles," *J. Mec.*, **5**, 245 (1966).

Dagan, Z., S. Weinbaum, and R. Pfeffer, "An Infinite Series Solution for the Creeping Motion Through an Orifice of Finite Length," *J. Fluid Mech.*, **115**, 505 (1982).

Fletcher, C. A. J., *Computational Fluid Dynamics*, Vol. 1, Springer-Verlag, New York (1991).

Goetz, D. J., M. E. el-Sabban, B. U. Pauli, and D. A. Hammer, "Dynamics of Neutrophil Rolling Over Stimulated Endothilium In Vitro," *Biophys. J.*, **66**, 2202 (1994).

Hollahan, J. R., and R. S. Rosler, "Plasma Deposition of Inorganic Thin Films," *Thin Film Processes*, J. L. Vossen and W. Kern, eds., Academic Press, New York (1978).

Hunt, J. B., and I. Torbe, "Characteristics of a Hydrostatic Thrust Bearing," *Int. J. Mech. Sci.*, **4**, 503 (1962).

Jackson, J. D., and G. R. Symmons, "An Investigation of Laminar Radial Flow Between Parallel Discs," *Appl. Sci. Res.*, **15**, 59 (1965).

Law, H.-S., and J. H. Masliyah, "Numerical Prediction of the Flow Field Due to a Confined Laminar Two-Dimensional Submerged Jet," *Comput. Fluids*, **12**, 199 (1984).

Lee, X. C., C. F. Ma, Q. Zheng, Y. Zhuang, and Y. Q. Tian, "Numerical Study of Recovery Effect and Impingement Heat Transfer with Submerged Circular Jets of Large Prandtl Number Liquid," *Int. J. Heat Mass Transfer*, **40**, 2647 (1997).

Lighthill, M. J., "Boundary Layer Theory," *Laminar Boundary Layers*, L. Rosenhead, ed., Dover, New York (1988).

Lin, Z. H., Y. J. Chou, and Y. H. Hung, "Heat Transfer Behaviors of a Confined Slot Jet Impingement," *Int. J. Heat Mass Transfer*, **40**, 1095 (1997).

Ma, C. F., Y. Zhuang, S. C. Lee, and T. Gomi, "Impingement Heat Transfer and Recovery Effect with Submerged Jets of Large Prandtl Number Liquid—II. Initially Laminar Confined Slot Jets," *Int. J. Heat Mass Transfer*, **40**, 1491 (1997).

Middleman, S., *Fundamentals of Polymer Processing*, McGraw-Hill, New York (1977).

Middleman, S., *Modeling Axisymmetric Flows: Dynamics of Films, Jets, and Drops*, Academic Press, New York (1995).

Moller, P. S., "Radial Flow Without Swirl Between Parallel Discs," *Aeronaut. Q.*, **14**, 163 (1963).

Raal, J. D., "Radial Source Flow Between Parallel Disks," *J. Fluid Mech.*, **85**, 401 (1978).

Reinberg, A. R., "Plasma Deposition of Inorganic Silicon Containing Films," *J. Electron. Mater.*, **8**, 345 (1979).

Roache, P. J., *Computational Fluid Dynamics*, Hermosa, Albuquerque, NM (1972).

Schafer, D. M., S. Ramadhyani, and F. P. Incropera, "Numerical Simulation of Laminar Convection Heat Transfer from an In-Line Array of Discrete Sources to a Confined Rectangular Jet," *Numer. Heat Transfer Part A*, **22**, 121 (1992).

Scholtz, M. T., and O. Trass, "Mass Transfer in a Nonuniform Impinging Jet: I. Stagnation Flow—Velocity and Pressure Distribution," *AIChE J.*, **16**, 82 (1970).

Sparrow, E. M., and L. Lee, "Analysis of Flow Field and Impingement Heat/Mass Transfer Due to a Nonuniform Slot Jet," *Trans. ASME J. Heat Transfer*, **97**, 191 (1975).

Vrentas, J. S., and J. L. Duda, "Flow of a Newtonian Fluid Through a Sudden Contraction," *Appl. Sci. Res.*, **28**, 241 (1973).

Watson, E. J., "The Radial Spread of a Liquid Jet over a Horizontal Plane," *J. Fluid Mech.*, **20**, 481 (1964).

Manuscript received Mar. 10, 1999, and revision received Sept. 17, 1999.